Lawrence Berkeley National Laboratory
Recent Work

Title
Cryogenic Laser Ablation Reveals Short-Circuit Mechanism in Lithium Metal Batteries

Authors
Jungjohann, KL
Gannon, RN
Goriparti, S
et al.

Cryogenic Laser Ablation Reveals Short-Circuit Mechanism in Lithium Metal Batteries

Katherine L. Jungjohann,* Renae N. Gannon, Subrahmanyam Goriparti, Steven J. Randolph, Laura C. Merrill, David C. Johnson, Kevin R. Zavadil, Stephen J. Harris, and Katharine L. Harrison

ACCESS | Metrics & More | Article Recommendations | Supporting Information

ABSTRACT: The dramatic 50% improvement in energy density that Li-metal anodes offer in comparison to graphite anodes in conventional lithium (Li)-ion batteries cannot be realized with current cell designs because of cell failure after a few cycles. Often, failure is caused by Li dendrites that grow through the separator, leading to short circuits. Here, we used a new characterization technique, cryogenic femtosecond laser cross sectioning and subsequent scanning electron microscopy, to observe the electroplated Li-metal morphology and the accompanying solid electrolyte interphase (SEI) into and through the intact coin cell battery's separator, gradually opening pathways for soft-short circuits that cause failure. We found that separator penetration by the SEI guided the growth of Li dendrites through the cell. A short-circuit mechanism via SEI growth at high current density within the separator is provided. These results will inform future efforts for separator and electrolyte design for Li-metal anodes.
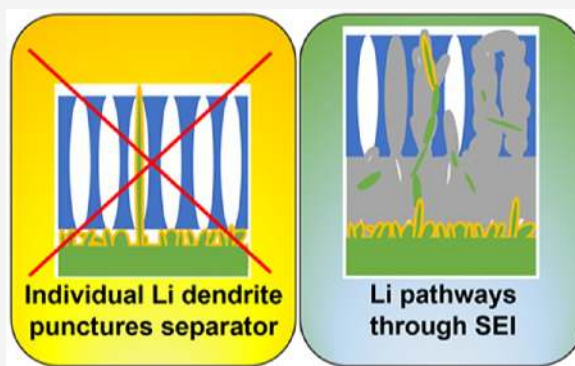
The demand for more energy-dense lithium-ion (Li-ion) batteries[1,2] is so intense that even small improvements are the subject of considerable research efforts. Replacing the graphite anode with a Li-metal anode results in an impressive 50% improvement in energy density;[3] however, Li-anode prototypes cycled at high energy density have consistently failed at low cycle numbers. The failure mechanisms are a matter of rigorous debate. The common theory postulates that ultimately failure lies with poorly controlled, electroplated Li-metal morphology, in the form of Li dendrites that can grow through the nanoscale tortuous pathway of the polymer separator.[4−7] However, the Monroe−Newman model, that neglects solid electrolyte interphase (SEI) properties, suggests that even large (>1 μm in diameter) dendrite formations cannot penetrate through the submicrometer diameter pores of the separator,[8] and recent cryogenic electron microscopy images have demonstrated that Li dendrites with submicrometer diameters are effectively deflected by the separator.[9] Therefore, the mechanism of how short circuits develop remains in question: if Li metal does not have the mechanical integrity to puncture through the porous separator, what is the pathway by which Li bridges the two electrodes through the separator?[10]

Alternatively, Li-anode failure has been attributed to the poor Li-ion transport properties of the SEI, a passivation film composed of organic and inorganic Li-containing species that forms during cell cycling.[4,11] The growth and propagation of SEI remains unclear because of the extreme difficulty of achieving unaltered, nanoscale characterization of the solid−liquid, air-sensitive, electrode−electrolyte interfaces. For example, microcomputed tomography (microCT) can acquire nondestructive structural images of the complete battery stack,[12,13] but only at ~700 nm resolution, and it cannot provide compositional mapping. In contrast, cryo-focused ion beam (FIB) preparation for cryo-scanning transmission electron microscopy provides nanoscale structural and compositional mapping,[14] but it can characterize sections only <50 μm^2 and the interfaces of interest must be severed during sample preparation, preventing representative and unperturbed imaging.

In this work, we demonstrate that high current densities cause soft shorts (parasitic electronic bridges in the cell), creating SEI inclusions within the separator that mechanically tear the separator and form open networks for Li-metal plating between the opposing electrodes. While Li metal is soft and
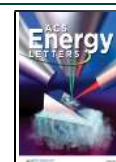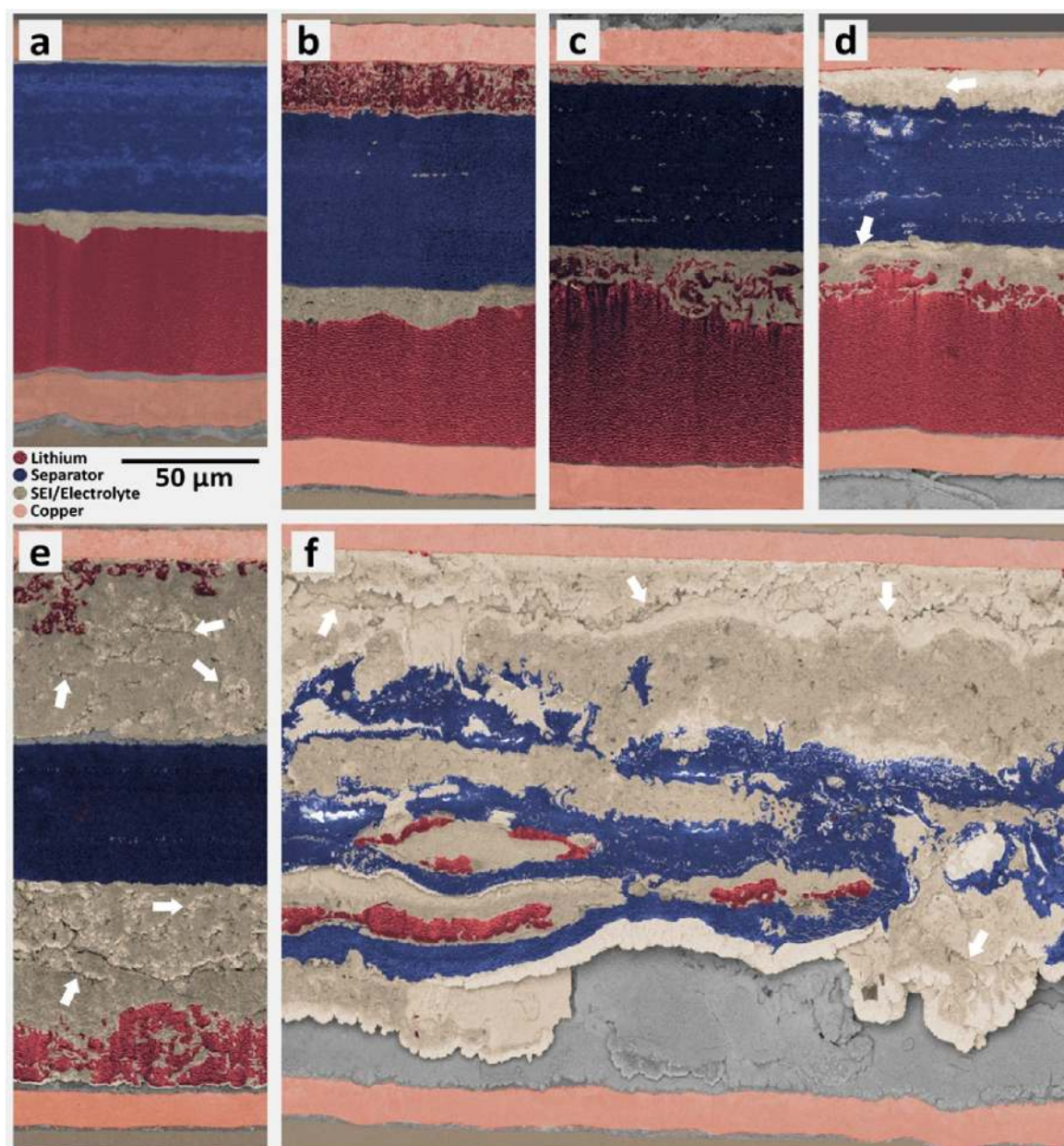
Figure 1. Scanning electron micrographs of intact angled-sections of high-rate cycled Li-metal half cells. (a) Uncycled cell, including: stainless-steel cap, Cu current collector, stack of two Celgard 2325 separators, Li metal, bottom Cu current collector, and lower stainless-steel disc, (b) 1st Li plating, (c) 1st Li stripping, (d) 11th plating, (e) 51st plating, and (f) 101st plating step. White arrows indicate cracks in the SEI matrix and gray regions indicate structures out-of-plane from the cut face.

should not be able to penetrate a separator, SEI capping and envelopment of the electroplated Li metal appears to aid in separator tearing. We have discovered this mechanism through the first implementation of a structural/compositional characterization method that captures nanoscale interactions between the different battery layers over representative cross sections, all without disassembling the battery stack along interfacial boundaries. Because our goal was to understand the interaction between the Li-metal anode and the separator (particularly at high rates that commonly lead to short circuits), we constructed half cells of 2032 coin cell batteries, each containing a 50 μm thick layer of Li-metal on a copper (Cu) foil counter electrode, with a 9 μm thick Cu current collector as the working electrode. The electrodes were stacked on either side of a pair of 25 μm thick trilayer Celgard 2325

separators for increased tortuosity; each separator had two polypropylene layers that sandwiched a central polyethylene layer.[15] Cells were cycled at a high rate of 1.88 mA/cm^2 to a capacity of 1.88 mAh/cm^2, so that we could observe changes in the Li metal/separator interfaces as a function of cycle number.

We characterized representative area (0.5 mm^2) samples from intact coin cells using a Helios laser plasma focused ion beam (Laser PFIB) system (Thermo Fisher Scientific, Figures S1−S3) to spatially map the Li-metal, polymer separator, volatile electrolyte [∼2.8 M lithium bis(fluorosulfonyl)imide in 1,2-dimethoxyethane],[16] and SEI layers. Sectioning was achieved using the athermal ultrashort pulse laser (UPL, removal rates >15 000× compared to a conventional Ga FIB) on the Laser PFIB tool.[17] This significant enhancement in material removal rates with the UPL was crucial to enabling

cross-sectioning through the coin cell casing (250 μm of stainless steel). To maintain the layers of the battery stack and volatile electrolyte in a solid state, the coin cell was placed in a custom, pretilted aluminum battery mount; the coin cell—mount assembly was frozen in liquid nitrogen, and the sample's temperature was controlled using a cryo-stage (<−100 °C, Figure S4).[18] Because of the angle between the mount and laser optical axis (Table S1), the SEM images are at the perspective of a 59°-angled section (Figure S5), and because the coin cell samples are flooded with excess electrolyte, varying quantities of electrolyte are visible between the top Cu and stainless-steel layers (Figure 1a,c). In Figure 1, the coin cell components are observed in the SEM images (Figures S6–S11; replicates of failure Figures S13–S17), where false color has been superimposed to reflect the energy dispersive X-ray spectroscopy (EDS) maps (Figures S18–S23). We observed a consistent increase in distance between the top and bottom Cu foils with increased cycling, as the mossy Li deposits and SEI grows with each plating and stripping step (Table S2). The correlation between cycling and SEI growth is a known phenomenon,[19] but the SEI's distribution and the extent of the growth were previously unquantifiable because ex situ measurements required the buried electrode/separator interfaces to be dismantled.

Our results show that copious SEI growth occurs over relatively few cycles at high-rate cycling. Even the first Li plating cycle (Figure 1b) shows that a fraction of the dark Li layer has moved across the separator and deposited on the Cu current collector at the top. A fully dense Li film should be only 9 μm thick, so the newly deposited 16 μm thick Li film must be either porous (filled in with electrolyte) and/or composed of both Li and SEI. Notably, small SEI deposits can already be observed within the separator, presumably resulting from conductive pathways (unresolved in these SEM images) that allowed small Li deposits to plate and react with electrolyte, forming these SEI inclusions.[20]

The first Li stripping cycle (Figure 1c) shows that after the Li is driven from the top Cu electrode, roughly 7 μm of SEI/electrolyte/dead-Li-residue remains, filling the region between the top Cu electrode and the separator. More pronounced SEI deposits are seen in the separator. Below the separator, Li plates on top of the fully dense Li-metal surface as a low-density matrix, coated in SEI and filled with electrolyte. By the 11th Li plating cycle (Figure 1d), there are small Li deposits on the top Cu electrode, and the far denser SEI matrix now causes deformation of the separator. Inclusions of large SEI deposits appear within the separator (on the scale of several micrometers), above an increasingly thick SEI layer and the roughened surface of the fully dense Li-metal layer. At the 51st Li-plating cycle (Figure 1e), the plated Li on the top Cu electrode again forms a low-density matrix of Li grains mixed with an extremely dense SEI matrix, which comprises most of the gap between the top Cu electrode and the separator. Interestingly, the separator retains its margins and structure, with only a few SEI inclusions. Below the separator, the electrolyte-filled SEI film is now much thicker than the fully dense Li-metal layer, which is being converted into a coarse SEI-filled network. At this point, there is clear evidence that copious SEI has formed by consuming large amounts of bulk active Li and electrolyte, with small embedded fragments of dead Li encased in the SEI.[20] Catastrophic cell failure is seen in the 101st plating cycle (Figure 1f), where the separator is completely shredded by SEI and large Li-metal deposits can be

seen within the separator's interior boundaries. These images repudiate the long-held assumption that a single Li dendrite spans the cell and creates a hard short; instead, these images indicate that the primary failure mechanisms are widespread SEI inclusions and separator shredding.

Our electrochemical data validates the structural/chemical maps, suggesting that the soft shorts formed during cycling caused the growth of SEI inclusions within the separator. As expected, the disintegration of the coin cell's internal structures coincided with the battery's obvious electrochemical failure, which we analyzed using chronopotentiometric data generated from cycling prior to Laser PFIB characterization (Figure S24, and replicates in Figures S26–S40). In the high rate cycled cells, the Coulombic efficiency measurements often exceed 100% and are likely indicative of soft short formation (Figure 2a,b). While random error or dead Li (stranding and reconnecting) could explain some of the variation shown
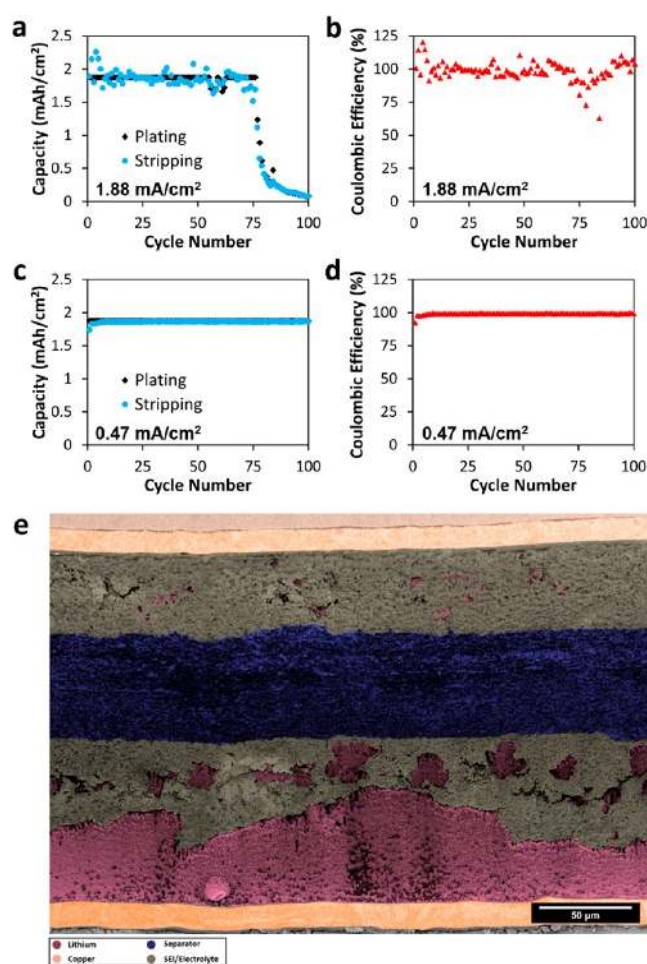

Figure 2. Electrochemical performance of the 101st Li plating sample. (a) Capacity of the plating and stripping cycles, for Li plating at a high rate of 1.88 mA/cm² up to the 101st plating step. (b) Coulombic efficiency of each full cycle, exhibiting the battery's ability to efficiently recapture Li, even after the quantity of plated Li significantly decreases at ~75 cycles. Capacity (c) and Coulombic efficiency (d) of the plating and stripping cycles at a low rate of 0.47 mA/cm² to a capacity of 1.88 mAh/cm². (e) Scanning electron micrograph of an intact angled-section of the 101st Li plating low-rate cycled half-cell. The brown layer at the top of the image is the stainless-steel cap, and the gray contrast indicates structures out-of-plane from the cut face.
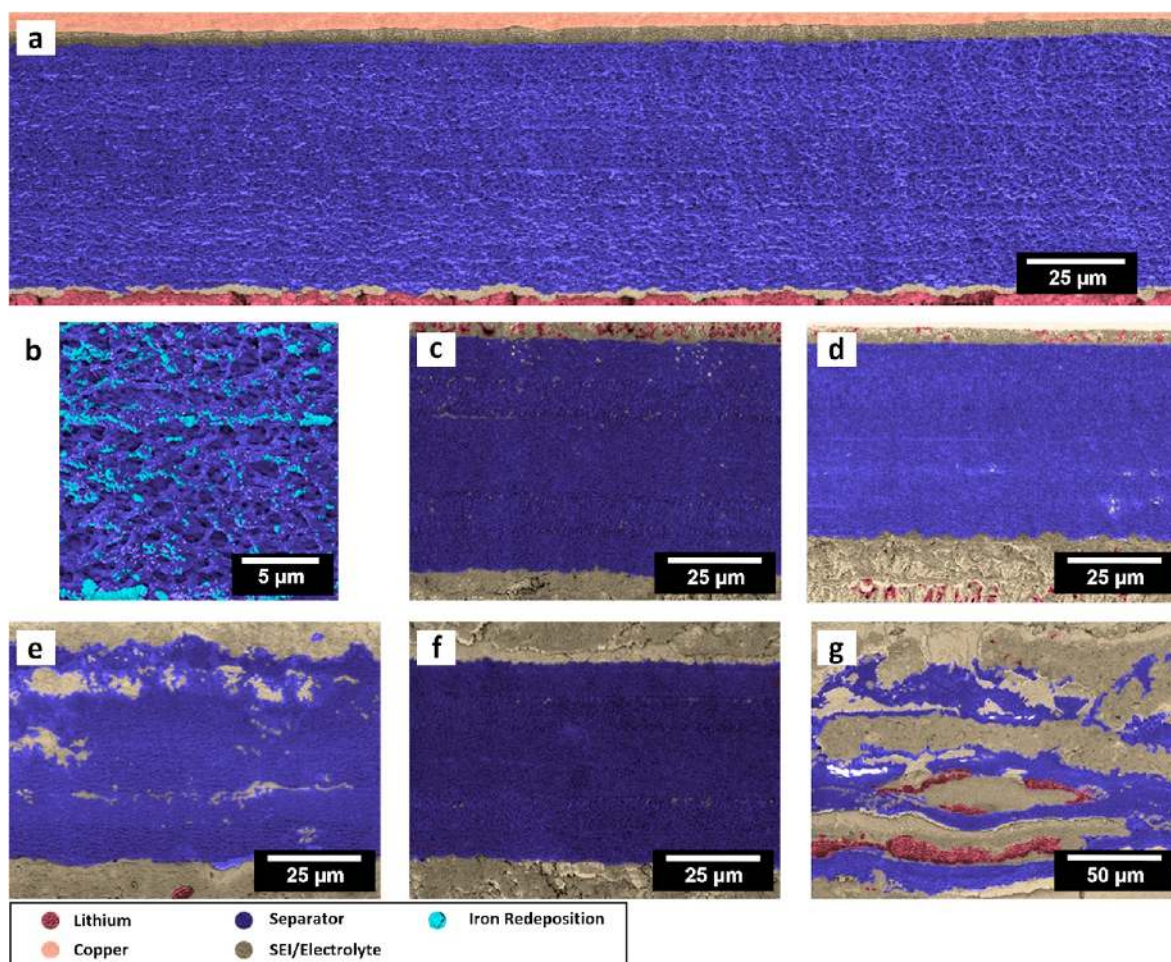
Figure 3. Scanning electron micrographs of high-rate cycled angled-sections showing failure within two stacked Celgard 2325 separators. (a) Uncycled cell and (b) higher-magnification image of the separator porosity (with the lighter contrast indicating iron redeposition from laser ablation), (c) 1st Li plating, (d) 1st Li stripping, (e) 11th plating, (f) 51st plating, and (g) 101st plating step.

above and below 100% Coulombic efficiency, the fact that the cumulative stripped capacity exceeds the cumulative plated capacity until cycle 46 strongly suggests that some of the charge passed is due to soft shorts. In the separator, widespread SEI inclusions indicate conductive paths (likely composed of small Li-metal fragments weakly connected in the SEI matrix),[20] which allow electron transport into the separator and enable the soft shorts.

A few cycles before the cell failed, the Coulombic efficiency dropped, likely indicating the cell's impending inability to plate to the specified capacity. However, after the cell began to fail, the Coulombic efficiency briefly recovered, which suggests that the loss in capacity is fundamentally decoupled from the loss in Coulombic efficiency. It should be noted that when the cell was unable to plate to the specified capacity, because of depletion of the accessible Li inventory (dead Li or blocked Li-transport pathways), the remaining Li inventory could still be efficiently cycled. This cell failed because of inaccessible or depleted Li inventory rather than from a hard short circuit caused by a dendrite.

Because most studies concentrate on low-rate cycling, the experiment was reproduced at 25% of the high-rate cycling to determine whether the same failure mechanisms pertained. Results (Figure 2c,d) demonstrate very steady capacity and Coulombic efficiency (>99%), even at high cycle numbers. At this lower current density, battery performance was very

repeatable from cell to cell and showed no signs of failure (Figure S25, and replicates in Figures S41–S43), which is consistent with the literature.[16] Furthermore, there appears to be a correlation between the observation of SEI and Li inclusions in the separator and the electrochemical data showing higher-than-expected stripping capacity, which we attribute to soft short formation. At the low-rate cycling, there was no significant oscillation around 100% Coulombic efficiency and the cumulative stripped capacity was always lower than the cumulative plated capacity. The SEM image (Figure S12) shows no evidence of SEI or Li inclusions in the separator at low-rate cycling (Figure 2e), which is consistent with the electrochemical data. Additionally, important differences between the high- and low-rate cycled 101st Li plating step coin cells can be seen in the separator structure, SEI thickness, plated Li-metal morphology, and the remaining counter-electrode Li thickness. Difference in the Li metal morphology may explain why less Li metal was consumed during the low-rate cycling. Visible cracks and crevices in the SEI may also indicate localized electrolyte consumption, which would reduce Li-ion transfer pathways during high-rate cycling.

Recent findings suggest that Coulombic efficiency is much more closely correlated to the quantity of inactive Li isolated from the current collector by SEI formation than to the amount of SEI formation.[20] This experiment validates that assumption because an abundant amount of SEI formed in the
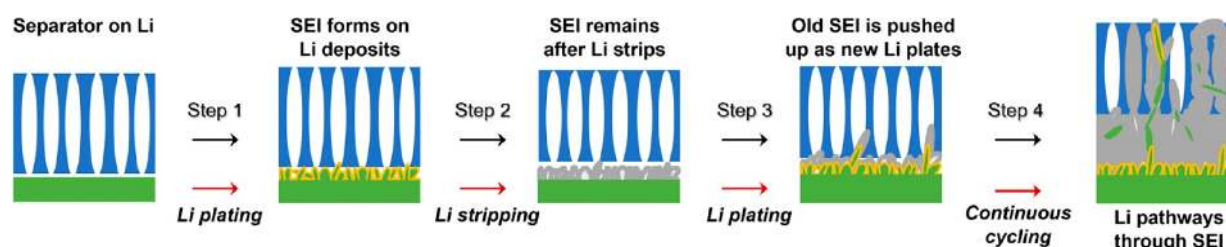
Figure 4. Schematic short-circuit mechanism for conductive Li pathways through the polymeric separator via SEI formation and subsequent deformation of the separator. SEI formed during the current plating step is colored yellow; SEI that formed in a prior step is colored gray.

high-rate cycled cells within just a few cycles, yet the depleted Li inventory did not cause an immediate drop in the very high Coulombic efficiency. The prevailing literature almost always attributes high-rate Li-metal anode cell failure to the formation of a single Li dendrite[21] that punches through separator pores in the battery stack.[22,23] However, our electrochemical data and cross-sectional images clearly demonstrate that the SEI forms inclusions within the separator, which gradually destroy the separator and create pathways for Li metal to plate within the separator.

Small SEI deposits protruding into the separator between the separator's polypropylene and polyethylene trilayers (Figure 3a,b) and small internal SEI inclusions (Figure 3c−f) can cause dramatic horizontal tearing along the trilayer interfaces (Figure 3g), creating compromised intertrilayer separator interfaces. This phenomenon demonstrates inadequate adhesion between the trilayers[24] and/or softening of the separator upon electrolyte saturation.[25] Large SEI inclusions also formed along the separator's top and bottom surfaces, punching vertically through the trilayers (Figure 3e), which resulted in further horizontal tearing. Because SEI formation can occur only with electrons at the required reduction potential, conductive paths (masked by SEI or too small to resolve in the SEM images) must be laced through the separator, providing all the components necessary to form SEI within the separator's trilayer structure (optical image in Figure S44). Under high-rate conditions, SEI formation in the separator can typically be observed very early in the Li-cycling process. Figure 3f (51st plating) shows few SEI inclusions compared to Figure 3e (11th plating), which demonstrates the stochastic nature of these processes, both within and among identically fabricated coin cells. However, while cell-to-cell variation was observed, many duplicate cells failed catastrophically between 75 and 100 cycles (Figures S13−S17 and S26−S40). Complete destruction of the trilayer separator before the 101st lithiation was evident in Figure 3g, clearly demonstrating that, for high-rate cycled Li-metal anodes, the trilayer separator was not mechanically sufficient to withstand SEI evolution.

Our full-stack nanoscale characterization points to a failure mechanism which had not been previously considered in theoretical modeling:[26] the SEI's mechanical properties create pathways that allow soft Li metal to penetrate into and tear the separator, with Li-metal plating providing the force for penetration (Figure 4). We believe that the extensive SEI formation is itself a product of the conductive pathways that form between the small Li-metal fragments embedded within the SEI. During the first plating step, some high-aspect ratio Li grains deposit and grow with a capping SEI film. We believe it is possible that the hard, sharp SEI tips can bore into the separator's small pores and even puncture the separator (results from carbonate electrolyte in Figures S45 and S46 and

alternative separator in Figures S47−S55). Once there is a complete conductive pathway through the separator, the cell-scale electronic bridge causes numerous soft shorts. More mechanically robust separators may mitigate this failure mode; however, uncontrolled SEI growth may still cause electrolyte redistribution and Li-ion transport blocking.

In summary, our structural images and elemental maps, paired with our electrochemical data, definitively indicate that degradation of the Li cycling performance is prompted by the destruction of ion-transport pathways between the stacked electrodes and consumption of Li metal by excessive SEI formation. Cycling causes the formation of small SEI inclusions with small Li-metal grains, creating delicate conductive pathways that form within the separator. These pathways cause numerous soft shorts, which then accelerate SEI formation causing physical disfigurement (and subsequently destroy) the separator's functionality. Although Li dendrites do not have the toughness to pierce the separator, the SEI can carve routes through the separator, opening pathways for more soft shorts by plating Li along those pathways. To prevent this from happening, future research must focus on minimizing SEI formation and improving the integrity of the separator for high-rate cycling Li-metal batteries. Our new characterization approach allows for nanoscale structural/chemical mapping of intact battery stacks without destroying the interfaces between the solid/liquid/polymer composite stack, preventing air or water vapor exposure that would otherwise alter the sensitive battery stack materials.

■ EXPERIMENTAL METHODS

Coin Cells. 2032-coin cells were fabricated with 16 mm diameter and 9 μm thick Cu current collectors as the working electrodes. The Cu was acid treated in 1.2 M hydrochloric acid for 10 min, washed with deionized water and acetone, dried, and then immediately transferred to an Ar-filled glovebox. The counter electrodes consisted of 16 mm diameter electrodes with 50 μm thick Li laminated to 10 μm thick Cu (Albemarle). Two layers of Celgard 2325 separators were placed between the two electrodes. The cells were flooded with 100 μL of ~2.8 M lithium bis(fluorosulfonyl)imide (LiFSI, Oakwood Chemicals) in 1,2-dimethoxyethane (DME, Sigma-Aldrich, anhydrous, 99.5%). The LiFSI salt was dried at 60 °C overnight in a heated antechamber connected to the glovebox. The DME was dried over activated alumina for at least 2 days before preparation of the electrolyte. The dry DME was extracted through a filter to remove any activated alumina; the DME and LiFSI were then mixed in a 2.4:1 molar ratio (DME:LiFSI) to make a ~ 2.8 M solution based on interpolation between previously documented electrolyte preparation procedures[16] The solution was stirred on a hot plate at 50 °C overnight. The cells were compressed with a precompressed wave spring and

1.8 mm total thickness of stainless streel spacers. The coin cells were allowed to rest for 24 h following fabrication before being tested on Biologic and Arbin battery cyclers. Coin cells were cycled at a current density of 1.88 or 0.47 mA/cm^2 to a capacity of 1.88 mAh/cm^2 during Li plating. A −1 V limit was programmed for plating, and stripping was allowed to continue until a voltage limit of 1 V was reached. A time limit was set to double the time required to strip the plated Li, so that if there was a short circuit, it would be easier to identify from higher-than-expected stripping capacity. Additional electrochemical data is presented in Figures S24 and S25 (with replicate cell data in Figures S26−S40 and S41−S43), detailing the voltage versus time curves for the cells imaged in Figure 1f and Figure 2e, respectively, with corresponding capacity and Coulombic efficiency data shown in Figures 2a,b and 2c,d, respectively.

Cryogenic Helios Laser PFIB. The Helios system was equipped with a cryogenic cooling stage from Quorum (Quorum Technologies, Newhaven, U.K.). Inherent sample size, geometry, and motion limitations were imposed using the cryogenic cooling stage in conjunction with the laser. Therefore, it was necessary to develop some nonstandard cross-sectioning techniques to access maximum sample area on the batteries and to allow better line-of-sight to the EDS detector. The experimental process consisted of coating the battery anodes with insulating paint (nail polish) then mechanically clamping them to a grounded, aluminum wedge via a copper clip. The mounting wedge was cut into a pretilt at −21° to accommodate for the limited negative tilt (toward the laser) on this prototype tool. Because the laser delivery was oriented 30 degrees from horizontal, the net cut-face angle into the batteries' surface was 51°, plus any additional negative stage tilt that was applied by the stage (Figure S4). The entire sample/stub was plunge frozen in liquid nitrogen for 15 min and then transferred in air to the precooled cryo-stage. Once the sample was mounted into the SEM chamber, immediate pumping to vacuum limited ice growth on the sample by the air. The precooled stage was kept at a temperature range between −100 °C and −120 °C during laser ablation and characterization.

Within the Helios, the sample was brought to eucentric height and the stage was tilted to −8° for laser processing. Figure S4 shows a schematic of this technique, which we call "oblique" cross-sectioning. Laser ablation followed a three-step procedure: (1) A large volume of material was removed using the 1030 nm laser at a large pulse energy and spot size. (2) The protective coverslip was replaced to allow more transmittance to the sample for polishing. (3) The cut face was polished using the 515 nm beam at a lower pulse energy and reduced pulse repetition rate (details in Table S1).

Image Processing. To highlight the different battery components, the SEM images were cropped and imported into Adobe Photoshop. Color layers were added to the assembly of images, where individual layers were representative of the different coin cell components: stainless steel, copper, separator, SEI/electrolyte, and Li metal. The identification of each region to color was guided by energy-dispersive X-ray spectroscopy maps (Figures S18−S23). The contribution of iron redeposition was removed from all the images, except for Figure 3b, to minimize distraction from focus on the configuration between the Li metal, separator, and SEI/electrolyte. We acknowledge that the iron redeposition was mostly observed in the high-rate 51st and 101st plating images, as the iron redeposition could not be removed from cracks and

crevices in the sample, which were caused by either factures in the SEI or gas evolution that resulted in a void during laser ablation.

■ ASSOCIATED CONTENT

ⓈI Supporting Information

The Supporting Information is available free of charge at https://pubs.acs.org/doi/10.1021/acsenergylett.1c00509.

> Complete discussion of the Helios Laser PFIB system and complementary Quorum cryo stage with sample milling and characterization details; all unprocessed images and EDS maps along with analysis of the electrochemical data and replicate samples; details of results obtained with a carbonate-based electrolyte with the Celgard 2325 separator and alternatively a Celgard 2400 separator with the 2.8 M LiFSI in DME electrolyte (PDF)

■ AUTHOR INFORMATION

Corresponding Author

    Katherine L. Jungjohann − *Center for Integrated Nanotechnologies, Sandia National Laboratories, Albuquerque, New Mexico 87185, United States;* ⓞ orcid.org/0000-0002-8132-1230; Email: kljungj@sandia.gov

Authors

    Renae N. Gannon − *Department of Chemistry, University of Oregon, Eugene, Oregon 97405, United States;* ⓞ orcid.org/0000-0002-8937-3262

    Subrahmanyam Goriparti − *Nanoscale Sciences, Sandia National Laboratories, Albuquerque, New Mexico 87185, United States*

    Steven J. Randolph − *Materials & Structural Analysis Division, Thermo Fisher Scientific, Hillsboro, Oregon 97124, United States*

    Laura C. Merrill − *Nanoscale Sciences, Sandia National Laboratories, Albuquerque, New Mexico 87185, United States;* ⓞ orcid.org/0000-0001-7673-4519

    David C. Johnson − *Department of Chemistry, University of Oregon, Eugene, Oregon 97405, United States;* ⓞ orcid.org/0000-0002-1118-0997

    Kevin R. Zavadil − *Nanoscale Sciences, Sandia National Laboratories, Albuquerque, New Mexico 87185, United States;* ⓞ orcid.org/0000-0002-3791-424X

    Stephen J. Harris − *Materials Science Division, Lawrence Berkeley National Laboratory, Berkeley, California 94720, United States*

    Katharine L. Harrison − *Nanoscale Sciences, Sandia National Laboratories, Albuquerque, New Mexico 87185, United States;* ⓞ orcid.org/0000-0002-5807-6919

Complete contact information is available at:
https://pubs.acs.org/10.1021/acsenergylett.1c00509

Notes
The authors declare no competing financial interest.

■ ACKNOWLEDGMENTS

■ REFERENCES

(1) Yoshino, A. The birth of the lithium-ion battery. *Angew. Chem., Int. Ed.* **2012**, *51* (24), 5798−5800.

(2) Yoshino, A.; Sanechika, K.; Nakajima, T. Secondary battery. US 4668595 A, 1987.

(3) Besenhard, J.; Eichinger, G. High energy density lithium cells: Part I. Electrolytes and anodes. *J. Electroanal. Chem. Interfacial Electrochem.* **1976**, *68* (1), 1−18.

(4) Fang, C.; Wang, X.; Meng, Y. S. Key issues hindering a practical lithium-metal anode. *Trends in Chemistry* **2019**, *1* (2), 152−158.

(5) Tikekar, M. D.; Choudhury, S.; Tu, Z.; Archer, L. A. Design principles for electrolytes and interfaces for stable lithium-metal batteries. *Nature Energy* **2016**, *1* (9), 16114.

(6) Xu, W.; Wang, J.; Ding, F.; Chen, X.; Nasybulin, E.; Zhang, Y.; Zhang, J.-G. Lithium metal anodes for rechargeable batteries. *Energy Environ. Sci.* **2014**, *7* (2), 513−537.

(7) Zhang, X.; Wang, Q. J.; Harrison, K. L.; Jungjohann, K.; Boyce, B. L.; Roberts, S. A.; Attia, P. M.; Harris, S. J. Rethinking how external pressure can suppress dendrites in lithium metal batteries. *J. Electrochem. Soc.* **2019**, *166* (15), A3639.

(8) Monroe, C.; Newman, J. Dendrite growth in lithium/polymer systems: A propagation model for liquid electrolytes under galvanostatic conditions. *J. Electrochem. Soc.* **2003**, *150* (10), A1377.

(9) Wang, H.; Liu, Y.; Li, Y.; Cui, Y. Lithium metal anode materials design: interphase and host. *Electrochemical Energy Reviews* **2019**, *2* (4), 509−517.

(10) Fincher, C. D.; Ojeda, D.; Zhang, Y.; Pharr, G. M.; Pharr, M. Mechanical properties of metallic lithium: from nano to bulk scales. *Acta Mater.* **2020**, *186*, 215−222.

(11) Peled, E.; Golodnitsky, D.; Ardel, G. Advanced model for solid electrolyte interphase electrodes in liquid and polymer electrolytes. *J. Electrochem. Soc.* **1997**, *144* (8), L208−L210.

(12) Frisco, S.; Liu, D. X.; Kumar, A.; Whitacre, J. F.; Love, C. T.; Swider-Lyons, K. E.; Litster, S. Internal Morphologies of Cycled Li-Metal Electrodes Investigated by Nano-Scale Resolution X-ray Computed Tomography. *ACS Appl. Mater. Interfaces* **2017**, *9* (22), 18748−18757.

(13) Shearing, P.; Brandon, N.; Gelb, J.; Bradley, R.; Withers, P.; Marquis, A.; Cooper, S.; Harris, S. Multi length scale microstructural investigations of a commercially available Li-ion battery electrode. *J. Electrochem. Soc.* **2012**, *159* (7), A1023.

(14) Zachman, M. J.; Tu, Z.; Choudhury, S.; Archer, L. A.; Kourkoutis, L. F. Cryo-STEM mapping of solid−liquid interfaces and dendrites in lithium-metal batteries. *Nature* **2018**, *560* (7718), 345.

(15) Zhang, X.; Sahraei, E.; Wang, K. Deformation and failure characteristics of four types of lithium-ion battery separators. *J. Power Sources* **2016**, *327*, 693−701.

(16) Qian, J.; Henderson, W. A.; Xu, W.; Bhattacharya, P.; Engelhard, M.; Borodin, O.; Zhang, J.-G. High rate and stable cycling of lithium metal anode. *Nat. Commun.* **2015**, *6*, 6362.

(17) Echlin, M. P.; Straw, M.; Randolph, S.; Filevich, J.; Pollock, T. M. The TriBeam system: Femtosecond laser ablation in situ SEM. *Mater. Charact.* **2015**, *100*, 1−12.

(18) Rahbani, J.; Behzad, A. R.; Khashab, N. M.; Al-Ghoul, M. Characterization of internal structure of hydrated agar and gelatin matrices by cryo-SEM. *Electrophoresis* **2013**, *34* (3), 405−408.

(19) Chen, K.-H.; Wood, K. N.; Kazyak, E.; LePage, W. S.; Davis, A. L.; Sanchez, A. J.; Dasgupta, N. P. Dead lithium: mass transport effects on voltage, capacity, and failure of lithium metal anodes. *J. Mater. Chem. A* **2017**, *5* (23), 11671−11681.

(20) Fang, C.; Li, J.; Zhang, M.; Zhang, Y.; Yang, F.; Lee, J. Z.; Lee, M.-H.; Alvarado, J.; Schroeder, M. A.; Yang, Y.; et al. Quantifying inactive lithium in lithium metal batteries. *Nature* **2019**, *572* (7770), 511−515.

(21) Lu, D.; Shao, Y.; Lozano, T.; Bennett, W. D.; Graff, G. L.; Polzin, B.; Zhang, J.; Engelhard, M. H.; Saenz, N. T.; Henderson, W. A.; et al. Failure mechanism for fast-charged lithium metal batteries with liquid electrolytes. *Adv. Energy Mater.* **2015**, *5* (3), 1400993.

(22) Lin, D.; Liu, Y.; Cui, Y. Reviving the lithium metal anode for high-energy batteries. *Nat. Nanotechnol.* **2017**, *12* (3), 194.

(23) Wang, W.; Hao, F.; Mukherjee, P. P. Mechanistics of Lithium-Metal Battery Performance by Separator Architecture Design. *ACS Appl. Mater. Interfaces* **2020**, *12* (1), 556−566.

(24) Kalnaus, S.; Wang, Y.; Turner, J. A. Mechanical behavior and failure mechanisms of Li-ion battery separators. *J. Power Sources* **2017**, *348*, 255−263.

(25) Gor, G. Y.; Cannarella, J.; Leng, C. Z.; Vishnyakov, A.; Arnold, C. B. Swelling and softening of lithium-ion battery separators in electrolyte solvents. *J. Power Sources* **2015**, *294*, 167−172.

(26) Bai, P.; Li, J.; Brushett, F. R.; Bazant, M. Z. Transition of lithium growth mechanisms in liquid electrolytes. *Energy Environ. Sci.* **2016**, *9* (10), 3221−3229.